nature photonics

ARTICLES

https://doi.org/10.1038/s41566-019-0348-z

Separation of valley excitons in a MoS_2 monolayer using a subwavelength asymmetric groove array

Liuyang Sun[1,10], Chun-Yuan Wang[1,2,10], Alex Krasnok[3,4], Junho Choi[1], Jinwei Shi[5], Juan Sebastian Gomez-Diaz[6], André Zepeda[1], Shangjr Gwo[2,7], Chih-Kang Shih[1], Andrea Alù[3,4,8,9*] and Xiaoqin Li[1*]

Excitons in monolayer transition metal dichalcogenides are formed at *K* and *K′* points at the boundary of the Brillouin zone. They acquire a valley degree of freedom, which has been explored as an alternative information carrier, analogous to charge or spin. Two opposite valleys in transition metal dichalcogenides can be optically addressed using light with different helicity. Here, we demonstrate that valley-polarized excitons can be sorted and spatially separated at room temperature by coupling a MoS_2 monolayer to a subwavelength asymmetric groove array. In addition to separation of valley excitons in real space, emission from valley excitons is also separated in photon momentum-space; that is, the helicity of photons determines a preferential emission direction. Our work demonstrates that metasurfaces can facilitate valley transport and establish an interface between valleytronic and photonic devices, thus addressing outstanding challenges in the field of valleytronics.

The extrema of the energy–momentum dispersion are called valleys[1–6]. Typically, it is difficult to control a particular valley because valleys do not exhibit unique coupling to an external field. An exception is found in monolayer transition metal dichalcogenides (TMDs), where the broken inversion symmetry combined with time-reversal symmetry causes opposite electron spins at the *K* and *K′* valleys, leading to an effective spin–valley locking[7–9], as illustrated in Fig. 1a. As a result, optical transitions such as excitons in opposite valleys can be excited selectively using light with different helicity, paving the way to an all-optical manipulation of the valley degree of freedom (DoF) and laying the foundations for the nascent field of valleytronics[1–3].

Separation of valley-polarized free carriers or excitons is a prerequisite to building valleytronic devices. Several previous experiments have explored different strategies to accomplish this goal. In the original theoretical proposal and first experimental demonstration of the free-carrier valley Hall effect in a MoS_2 monolayer[2,10], the Berry curvature of the energy band acts as a momentum-dependent magnetic field. Analogous to the Hall effect, electrons driven by an in-plane electric field undergo a valley-dependent transverse deflection perpendicular to both the electric and effective magnetic fields. Recently, the exciton valley Hall effect in monolayer MoS_2 was reported[11], where excitons in opposite valleys are separated in the transverse direction in the presence of a temperature gradient[11]. However, strain accidentally introduced in the sample preparation process may have also contributed to valley exciton separation. These demonstrations of valley Hall effects were performed at low temperature, placing an undesirable limitation on practical applications. A prominent feature associated with excitons in TMD monolayers is an exceptionally large binding energy, in the range of a few hundred meV, partially due to insufficient dielectric screening outside the extremely thin layers[12–16]. Such a large exciton binding energy should enable room-temperature operation of valleytronic devices.

In this Article we demonstrate that a suitably designed plasmonic metasurface consisting of an array of subwavelength asymmetric grooves effectively sorts and separates valley excitons in a MoS_2 monolayer at room temperature (Fig. 1b). This valley index separation is facilitated by near-field coupling between excitons and guided surface plasmon polariton (gSPP) modes propagating along the grooves[17–20]. Regardless of the excitation condition, no valley polarization in a MoS_2 monolayer is present at room temperature. Thus, our approach is rather general and applicable to a wide range of materials. Furthermore, photons with definite chirality emitted by valley excitons are separated in momentum space, enabling far-field optical detection of valley excitons. Therefore, the metasurface also serves as an interface between valleytronics and photonic devices.

Results and discussion

Unidirectional launching of SPPs based on the photonic spin Hall effect has been demonstrated previously at a metal–dielectric interface and in metamaterials[21–24]. Specifically, opposite circularly polarized dipoles have been shown to excite SPPs propagating in opposite directions. So far, however, all these previous demonstrations have focused on circularly polarized dipoles with an out-of-plane orientation. Such a perpendicular dipole couples to the transverse-magnetic (TM) polarized SPPs propagating along the plasmonic interfaces. In contrast, bright excitons at the *K* and *K′* valleys in monolayer MoS_2 possess only in-plane circular polarization ($E_x \pm iE_y$), oscillating with opposite helicity (Fig. 1a)[25]. These dipoles oriented in-plane cannot asymmetrically excite conventional SPPs, because they do not engage the required out-of-plane chiral response. Thus, it is necessary to specifically design

[1]Department of Physics, Complex Quantum Systems, and Texas Materials Institutes, University of Texas at Austin, Austin, TX, USA. [2]Department of Physics, National Tsing-Hua University, Hsinchu, Taiwan. [3]Department of Electrical and Computer Engineering, The University of Texas at Austin, Austin, TX, USA. [4]Photonics Initiative, Advanced Science Research Center, City University of New York, New York, NY, USA. [5]Department of Physics and Applied Optics Beijing Area Major Laboratory, Beijing Normal University, Beijing, China. [6]Department of Electrical and Computer Engineering, University of California, Davis, Davis, CA, USA. [7]Research Center for Applied Sciences, Academia Sinica, Nankang, Taipei, Taiwan. [8]Physics Program, Graduate Center, City University of New York, New York, NY, USA. [9]Department of Electrical Engineering, City College of The City University of New York, New York, NY, USA. [10]These authors contributed equally: Liuyang Sun, Chun-Yuan Wang. *e-mail: aalu@gc.cuny.edu; elaineli@physics.utexas.edu

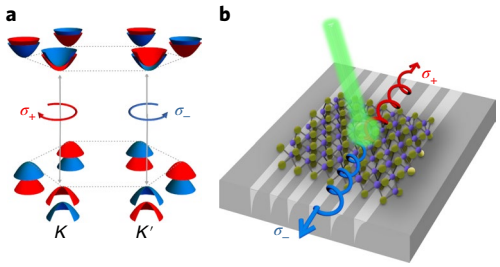

Fig. 1 | Schematics of optically addressable valleys and spatial separation of valley excitons by a metasurface. a, Schematics of the band structure and optical selection rules of excitons in monolayer MoS_2. σ_+ (σ_-) polarized light excites excitons in the K (K') valley. **b**, Illustration of valley excitons separation in real space by coupling a MoS_2 monolayer to a metasurface consisting of subwavelength asymmetric grooves. In addition, emission of excitons from opposite valleys are separated in photon momentum space.

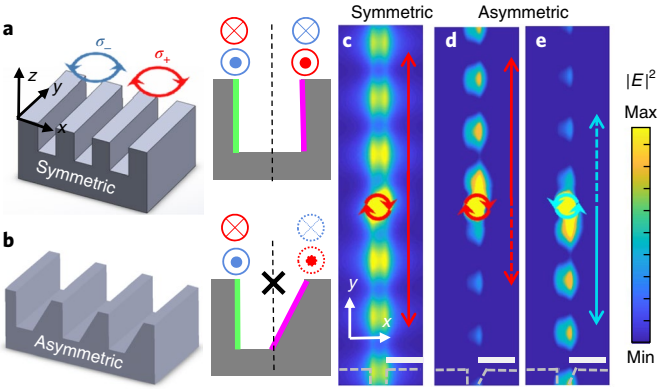

Fig. 2 | Metasurface design principle. a,**b**, Illustration of the gSPPs excited by circularly polarized light in symmetric (**a**) and asymmetric (**b**) grooves. On the left wall, gSPPs excited by a σ_+ (σ_-) dipole propagate into (out of) the page. On the right wall, the direction of propagation reverses. For a symmetric grating, no chirality-dependent gSPP propagation is observed due to the mirror symmetry indicated by the dashed black line. The mirror symmetry is lifted for an asymmetric groove, resulting in chiral-dependent gSPP propagation. **c**,**d**, Simulated electric field intensity distribution induced by a σ_+ dipole on a symmetric (**c**) and an asymmetric (**d**) grating. **e**, Electric field intensity distribution induced by a σ_- dipole on the asymmetric grating. Grey dashed lines in **c**–**e** indicate the positions of the side walls. Red (blue)-arrowed solid lines indicate the preferred propagation direction of σ_+ (σ_-) polarized gSPP. White scale bar in **c**–**e**, 200 nm.

metasurfaces that can break the chiral symmetry within the plane and ensure good coupling efficiency between excitons and gSPPs.

We have designed an array of subwavelength asymmetrically shaped grooves (Fig. 2). Each groove supports gSPP propagation along its side walls. In the case of an array of symmetric grooves (Fig. 2a), mirror symmetry along the y–z plane (dashed black curve) leads to chirality-independent propagation. In other words, an in-plane dipole with either left- or right-handed chirality couples to both side walls equally. However, if the mirror symmetry is intentionally broken by tilting one side wall (Fig. 2b), the gSPPs excited by a circularly polarized in-plane dipole on the two side walls differ. As a result, a σ_+ (σ_-) dipole preferentially excites gSPPs propagating upward (downward), as shown in Fig. 2d,e. (For more details see Supplementary Section 1). Thus, this concept enables chirality-dependent coupling between valley excitons in TMD monolayers and the designed metasurface, extending the previous demonstrations of the photonic spin-Hall effect. Figure 2c–e compares the calculated spatial distribution of electric field intensity for a metasurface with symmetric and asymmetric grooves. The excitation source used in the calculation is a circularly polarized in-plane dipole placed in the middle of a groove. The groove array with subwavelength period enables better spectral overlap between the SPP resonance and the MoS_2 excitons, thus boosting the SPP–exciton coupling efficiency. More importantly, the periodic array separates the valley excitons along a well-defined direction regardless of the excitation laser position on the metasurface. In comparison, a recent demonstration of valley exciton separation was based on coupling a few-layer-thick WS_2 flake to a single nanowire[26]. In this case, the direction of valley separation depends sensitively on the position of the excitation laser spot relative to the nanowire, making this method less practical.

The metasurface was fabricated using focused ion beam (FIB) milling on high-quality silver plates grown by a chemical synthesis method developed by us[27]. A scanning electron microscope image from a region of the metasurface is shown in Fig. 3a. The asymmetric grooves are fabricated in two FIB steps, leading to two different depths ($d_1 = 150$ nm and $d_2 = 90$ nm) and a total width (w) of 90 nm. The depth, width and period (200 nm) determine the spectral position of the surface plasmon resonance (Supplementary Section 2). These dimensions are chosen such that the gSPP spectrum may overlap with the absorption and emission wavelengths of excitons in MoS_2 at room temperature. Furthermore, these parameters are close to optimal to maximize the gSPP propagation distance and valley exciton separation (Supplementary Section 3). After FIB milling, a conformal Al_2O_3 layer (~5 nm thick) was deposited using atomic layer deposition to protect the silver metasurface structures. A perfectly smooth tilted side wall cannot be created using FIB due to the Ga ion beam shape. We demonstrate that the exact shape of the asymmetric side walls is not critical to observing the phenomenon by comparing results from two metasurfaces with different side wall shapes (Supplementary Section 4). The similar results obtained for the two fabricated metasurfaces show that the main cause of valley selectivity is the overall asymmetry of the grooves[20].

The MoS_2 monolayer was prepared by mechanical exfoliation and then transferred onto the metasurface. Part of the monolayer MoS_2 covered the groove array, while part of the monolayer was on top of the unstructured silver film (Supplementary Section 5). Measurements were taken from both regions for comparison. We refer to measurements taken on the smooth silver surface as a control experiment. We first took photoluminescence spectra using a circularly polarized excitation laser centred at 532 nm and observed an exciton resonance centred at 650 nm. The spectral position of the exciton resonance is consistent with A excitons in monolayer MoS_2 at room temperature. Trions cannot be spectrally distinguished from excitons at room temperature because the linewidth exceeds the trion binding energy. It was shown in previous experiments that a MoS_2 monolayer excited by a σ_+ polarized laser preferentially emits photons with σ_+ helicity at cryogenic temperature[7–9,28]. The degree of valley polarization is quantified as $\rho_\omega = \frac{I_+(\omega) - I_-(\omega)}{I_+(\omega) + I_-(\omega)}$, where I_+ (I_-) refers to the photoluminescence intensity with σ_+ (σ_-) polarization at the peak of the exciton resonance and ω is the spectral frequency. Exciton valley polarization strongly depends on the excitation laser wavelength and temperature[7–9,28]. With an excitation laser at 532 nm and at room temperature, we do not observe any exciton valley polarization, consistent with previous experiments (Supplementary Section 6). By placing MoS_2 on top of a metasurface, it is not only valley excitons that are separated in real space; emitted photons with different helicity are also separated in momentum space, as we demonstrate in the following. We use r and k to represent real space and photon momentum space, respectively.

We chose to populate the two valleys equally by using an excitation laser with linear polarization perpendicular to the groove. The local electric field along the groove edges was enhanced, leading to

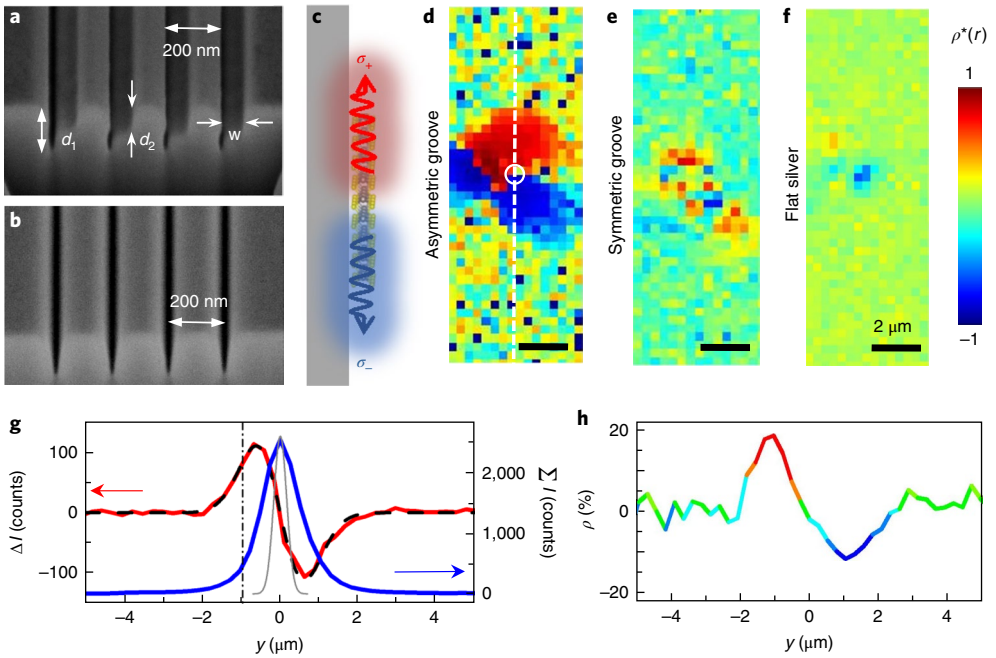

Fig. 3 | Experimental observation of separation of valley excitons in real space. a,**b**, Scanning electron microscope image of asymmetric grooves (**a**) and symmetric grooves (**b**). **c**, Illustration of valley exciton separation in real space. **d**–**f**, Colour plots of valley polarization contrast $\rho^*(r)$ in real space measured for a MoS_2 asymmetric groove array (**d**), a MoS_2 symmetric groove array (**e**) and a MoS_2 flat silver film (**f**). The white circle in **d** illustrates the position and spot size of the excitation. **g**, Line profiles of ΣI (blue) and ΔI (red) with dark counts removed along the vertical white dashed line in **d**. The black dashed line is a fitting curve obtained after subtracting two Gaussian envelopes. The peak-to-peak distance is 1.4 μm. The vertical dash-dotted line indicates the position of maximal ρ. The grey curve indicates the profile of the excitation laser. **h**, A line profile ρ shows that the maximal valley polarization reaches 18%.

increased absorption by the monolayer. The spatial profile of the photoluminescence from the MoS_2 monolayer on a metasurface, the monolayer on a smooth silver surface and the excitation laser itself were all captured by a charge-coupled device (CCD) camera following a spectrometer. We selected the σ_+/σ_- photoluminescence by placing a series of polarizers and waveplates in the detection path. The σ_+ and σ_- photoluminescence images were taken separately. The difference between the two spectra was then divided by their sum to obtain a spatial image of valley polarization. Figure 3d shows the measured valley polarization from the MoS_2–metasurface hybrid structure, where a spatial separation of valley excitons is clearly observed.

For comparison, we also prepared a hybrid structure with MoS_2 on a metasurface with symmetric grooves. Figure 3b presents a cross-section of the symmetric grooves in this second sample. As expected, we did not observe a regular spatial pattern of valley polarization (Fig. 3e). Small fluctuations are probably due to deviations from perfectly symmetric grooves, as designed. In another control experiment, we measured the same emission pattern on MoS_2 on an unstructured silver film. Again, no detectable valley polarization was observed from this hybrid structure (Fig. 3f). These two control experiments confirmed that the valley exciton separation originates from coupling to the gSPP propagation along asymmetric grooves.

To quantify the spatial valley polarization, we analysed the differential intensity $\Delta I(y) = I_+(y) - I_-(y)$ and sum intensity $\Sigma I(y) = I_+(y) + I_-(y)$ along the white dashed line parallel to the groove direction (y), which are shown in Fig. 3g as red and blue curves, respectively. The ΔI profile can be fitted well by subtracting two Gaussian functions centred at $y = \pm 0.7$ μm, respectively (dashed black curve in Fig. 3g). Considering the finite laser spot size (~0.4 μm full-width at half-maximum) using a deconvolution process, the valley exciton separation was retrieved to be ~1.2 μm. The normalized valley polarization $\rho = \Delta I/\Sigma I$ is plotted in Fig. 3h, yielding a maximum valley polarization of ~18%. (For data analysis see Methods).

We now discuss the mechanism underlying the valley exciton separation. Three different processes can lead to exciton emission, while the only process that enables valley exciton separation relies on a near-field non-radiative energy transfer of exciton–gSPP–exciton[29] (Supplementary Section 7). Through detailed simulations (presented in Supplementary Section 8), we estimate a total efficiency for the exciton–gSPP–exciton conversion process to be ~22%. The gSPPs critical in routing valley excitons are confined within the grooves and do not radiate to the far field without first transferring their energy to excitons. The spatial separation between valley excitons (~1.2 μm) is limited by the relatively short gSPP propagation distance imposed by the present metasurface design, non-ideal FIB fabrication processes and loss in the silver. In our experiment, the exciton diffusion measured for the MoS_2 monolayer on the unstructured silver film is similar to the gSPP propagation distance. Thus, excitons directly excited by the laser diffuse and contribute to a background signal, leading to reduced valley polarization. Both the separation distance and the degree of valley polarization can be improved with a different metasurface design (Supplementary Section 9). gSPPs scattered by defects may also contribute to the background signal in principle. However, this scattering of the signal by random defects should neither preserve chirality nor form distinct spatial patterns. In addition, the high-quality single-crystalline silver substrate used in the current experiments ensures that this scattering is greatly suppressed[27] (Supplementary Section 10).

In addition to valley exciton spatial separation, we also expect the emitted chiral photons to be separated in momentum space. Such a separation is desirable for interfacing valleytronic and photonic devices. Completely independent of the real-space localization

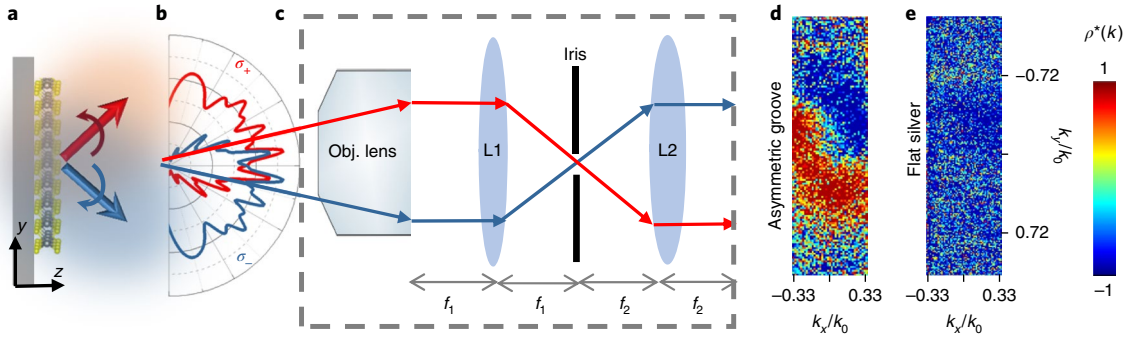

Fig. 4 | Experimental observation of valley exciton emission separation in momentum space. a, Illustration of excitons from opposite valleys emitting photons in different directions. **b**, Numerical simulations showing that the metasurface guides photons of opposite helicity preferentially towards the upper and lower hemispheres. **c**, Schematics of the set-up used to record photoluminescence images in photon momentum space. **d**,**e**, Colour plots of valley polarization contrast $\rho^*(k_{||})$ obtained from MoS_2 metasurface (**d**) and MoS_2 unstructured silver film (**e**). The maximal $\rho(k_{||})$ extracted is 8% after removing dark counts.

of the exciton, the asymmetric grooves shape the emission pattern of an in-plane dipole. The emitted photons are emitted to different directions according to their chirality, as illustrated in Fig. 4a. The calculated polarization-resolved far-field pattern (Fig. 4b) shows that σ_+ and σ_- polarized photons from opposite valleys preferentially emit towards the upper and lower hemisphere (Supplementary Section 11). The separation of photon emissions from valley-polarized excitons has been demonstrated by others using different metasurface designs[30,31]. In one such previous experiment, exciton–plasmon polaritons supported on a metasurface with rotated rectangular nanoapertures were shown to exhibit chirality-dependent emissions[30].

We define $\rho(k_{||})$ to quantify the chirality-dependent emission pattern. Here, $k_{||}=k_0\sin\theta$ is the momentum component of light parallel to the x–y plane, $k_0=2\pi/\lambda$ is the wavevector of light at wavelength λ in free space, and θ is the angle between k_0 and the x–y plane. Experimentally, we obtained $\rho(k_{||})$ by the k-space imaging technique. The set-up is sketched in Fig. 4c and explained in detail in the Methods. Similarly, the $\rho(k_{||})$ is obtained by taking the k-space images of σ_+ and σ_- emissions separately. The ratio $\rho^\star$ between the difference and sum of the two images from monolayer MoS_2 on the metasurface is plotted in Fig. 4d. The sign of $\rho^*(k_{||})$ reverses at opposite sides of the k space, demonstrating that the metasurface leads to directional emission of chiral photons. The maximum $\rho(k_{||})$ calculated with dark counts removed is 8%. In contrast, $\rho(k_{||})$ is negligible across the whole k space for photons emitted by monolayer MoS_2 placed on a smooth silver surface, as shown in Fig. 4e.

In our experiments, the total exciton population is balanced in the two valleys if the signal is integrated in either the real space or momentum space. This balance results from linear polarization excitation and is consistent with the photoluminescence spectra shown in Supplementary Fig. 1. The fact that valley polarizations are different in real space and momentum space reflects the capability of the metasurface to separate the valley excitons in both domains, opening exciting opportunities to manipulate valley excitons and their emission in both the near and far fields.

Conclusions

In summary, we have demonstrated the sorting and routing of valley-polarized excitons in a MoS_2 monolayer at room temperature with a metasurface. Our method is based on an array of subwavelength asymmetric grooves that can separate gSPPs with different chirality. Via non-radiative energy transfer between gSPPs and excitons, excitons in opposite valleys are separated in real space. Unlike previous studies[26], our approach is generally applicable to atomically thin materials that do not exhibit any valley polarization at room temperature. The degree of valley polarization can be significantly enhanced by optimizing the metasurface design. Enhanced valley polarization separation can also be achieved using excitons with a dipole orientation perpendicular to the two-dimensonal plane (see Supplementary Section 12 for an example), commonly found in TMD heterostructures or dark excitons in monolayers[32–36]. The combination of metasurfaces as passive components and two-dimensonal materials as active components will enable the creation of hybrid photonic devices for controlling exciton/spin/valley transport and the engineering of quantum emitter arrays[37–43].

Online content

Any methods, additional references, Nature Research reporting summaries, source data, statements of data availability and associated accession codes are available at https://doi.org/10.1038/s41566-019-0348-z.

Received: 1 August 2018; Accepted: 21 December 2018;
Published online: 11 February 2019

References

1. Xu, X., Yao, W., Xiao, D. & Heinz, T. F. Spin and pseudospins in layered transition metal dichalcogenides. *Nat. Phys.* **10**, 343–350 (2014).
2. Xiao, D. et al. Coupled spin and valley physics in monolayers of MoS_2 and other group-VI dichalcogenides. *Phys. Rev. Lett.* **108**, 196802 (2012).
3. Schaibley, J. R. et al. Valleytronics in 2D materials. *Nat. Rev. Mater.* **1**, 16055 (2016).
4. Gunawan, O. et al. Valley susceptibility of an interacting two-dimensional electron system. *Phys. Rev. Lett.* **97**, 186404 (2006).
5. Shkolnikov, Y., De Poortere, E., Tutuc, E. & Shayegan, M. Valley splitting of AlAs two-dimensional electrons in a perpendicular magnetic field. *Phys. Rev. Lett.* **89**, 226805 (2002).
6. Rycerz, A., Tworzydło, J. & Beenakker, C. Valley filter and valley valve in graphene. *Nat. Phys.* **3**, 172–175 (2007).
7. Mak, K. F., He, K., Shan, J. & Heinz, T. F. Control of valley polarization in monolayer MoS_2 by optical helicity. *Nat. Nanotechnol.* **7**, 494–498 (2012).
8. Zeng, H. et al. Valley polarization in MoS_2 monolayers by optical pumping. *Nat. Nanotechnol.* **7**, 490–493 (2012).
9. Cao, T. et al. Valley-selective circular dichroism of monolayer molybdenum disulphide. *Nat. Commun.* **3**, 887 (2012).
10. Mak, K. F., McGill, K. L., Park, J. & McEuen, P. L. The valley Hall effect in MoS_2 transistors. *Science* **344**, 1489–1492 (2014).
11. Onga, M., Zhang, Y., Ideue, T. & Iwasa, Y. Exciton Hall effect in monolayer MoS_2. *Nat. Mater.* **16**, 1193–1197 (2017).
12. Mak, K. F. et al. Tightly bound trions in monolayer MoS_2. *Nat. Mater.* **12**, 207–211 (2013).
13. Ross, J. S. et al. Electrical control of neutral and charged excitons in a monolayer semiconductor. *Nat. Commun.* **4**, 1474 (2013).
14. Berkelbach, T. C., Hybertsen, M. S. & Reichman, D. R. Theory of neutral and charged excitons in monolayer transition metal dichalcogenides. *Phys. Rev. B* **88**, 045318 (2013).

15. Lui, C. et al. Trion-induced negative photoconductivity in monolayer MoS_2. *Phys. Rev. Lett.* **113**, 166801 (2014).
16. Singh, A. et al. Trion formation dynamics in monolayer transition metal dichalcogenides. *Phys. Rev. B* **93**, 041401 (2016).
17. Novikov, I. V. & Maradudin, A. A. Channel polaritons. *Phys. Rev. B* **66**, 035403 (2002).
18. Pile, D. F. & Gramotnev, D. K. Channel plasmon–polariton in a triangular groove on a metal surface. *Opt. Lett.* **29**, 1069–1071 (2004).
19. Volkov, V. S. et al. Nanofocusing with channel plasmon polaritons. *Nano Lett.* **9**, 1278–1282 (2009).
20. Söllner, I. et al. Deterministic photon–emitter coupling in chiral photonic circuits. *Nat. Nanotechnol.* **10**, 775–778 (2015).
21. Kapitanova, P. V. et al. Photonic spin Hall effect in hyperbolic metamaterials for polarization-controlled routing of subwavelength modes. *Nat. Commun.* **5**, 3226 (2014).
22. Mueller, J. B. & Capasso, F. Asymmetric surface plasmon polariton emission by a dipole emitter near a metal surface. *Phys. Rev. B* **88**, 121410 (2013).
23. Rodríguez-Fortuño, F. J. et al. Near-field interference for the unidirectional excitation of electromagnetic guided modes. *Science* **340**, 328–330 (2013).
24. Lin, J. et al. Polarization-controlled tunable directional coupling of surface plasmon polaritons. *Science* **340**, 331–334 (2013).
25. Schuller, J. A. et al. Orientation of luminescent excitons in layered nanomaterials. *Nat. Nanotechnol.* **8**, 271–276 (2013).
26. Gong, S.-H. et al. Nanoscale chiral valley–photon interface through optical spin–orbit coupling. *Science* **359**, 443–447 (2018).
27. Wang, C.-Y. et al. Giant colloidal silver crystals for low-loss linear and nonlinear plasmonics. *Nat. Commun.* **6**, 7734 (2015).
28. Sallen, G. et al. Robust optical emission polarization in MoS_2 monolayers through selective valley excitation. *Phys. Rev. B* **86**, 081301 (2012).
29. Shi, J. et al. Cascaded exciton energy transfer in a monolayer semiconductor lateral heterostructure assisted by surface plasmon polariton. *Nat. Commun.* **8**, 35 (2017).
30. Chervy, T. et al. Room temperature chiral coupling of valley excitons with spin–momentum locked surface plasmons. *ACS Photon.* **5**, 1281–1287 (2018).
31. Guddala, S. et al. Valley selective optical control of excitons in 2D semiconductors using chiral metasurface. Preprint at https://arXiv.org/abs/1811.00071 (2018).
32. Zhou, Y. et al. Probing dark excitons in atomically thin semiconductors via near-field coupling to surface plasmon polaritons. *Nat. Nanotechnol.* **12**, 856–860 (2017).
33. Malic, E. et al. Dark excitons in transition metal dichalcogenides. *Phys. Rev. Mater.* **2**, 014002 (2018).
34. Ye, Z. et al. Probing excitonic dark states in single-layer tungsten disulphide. *Nature* **513**, 214–218 (2014).
35. Park, K.-D. et al. Radiative control of dark excitons at room temperature by nano-optical antenna-tip Purcell effect. *Nat. Nanotechnol.* **13**, 59–64 (2018).
36. Yu, H., Liu, G.-B. & Yao, W. Brightened spin–triplet interlayer excitons and optical selection rules in van der Waals heterobilayers. *2D Mater.* **5**, 035021 (2018).
37. Ziwei, L. et al. Tailoring MoS_2 valley-polarized photoluminescence with super chiral near-field. *Adv. Mater.* **30**, 1801908 (2018).
38. Yu, H. et al. Moiré excitons: from programmable quantum emitter arrays to spin–orbit-coupled artificial lattices. *Sci. Adv.* **3**, e1701696 (2017).
39. Aieta, F., Kats, M. A., Genevet, P. & Capasso, F. Multiwavelength achromatic metasurfaces by dispersive phase compensation. *Science* **347**, 1342–1345 (2015).
40. Su, X. et al. Negative reflection from metal/graphene plasmonic gratings. *Opt. Lett.* **41**, 348–351 (2016).
41. Asadchy, V. S. et al. Perfect control of reflection and refraction using spatially dispersive metasurfaces. *Phys. Rev. B* **94**, 075142 (2016).
42. Yin, X. et al. Photonic spin Hall effect at metasurfaces. *Science* **339**, 1405–1407 (2013).
43. Tran, K. et al. Moiré excitons in van der Waals heterostructures. Preprint at https://arXiv.org/abs/1807.03771 (2018).

Acknowledgements

L.S., A.Z., C.-K.S. and X.L. were supported by NSF EFMA-1542747 and NSF DMR-1306878. J.C., C.-K.S., X.L. and A.A. are supported by NSF MRSEC programme DMR-1720595. X.L. also acknowledges support from the Welch Foundation via grant F-1662. A.A., A.K. and J.S.G.-D. were partially supported by the Air Force Office of Scientific Research (MURI grant no. FA9550-17-1-0002), the DARPA Nascent program and the Welch Foundation (grant no. F-1802). S.G. and C.-Y.W. acknowledge support from the Ministry of Science and Technology (MOST) in Taiwan (MOST 105-2112-M-007-011-MY3). Collaboration between National Tsing-Hua University and The University of Texas at Austin is facilitated by the Global Networking Talent (NT 3.0) Program, Ministry of Education in Taiwan. J.S.G.-D. is supported by NSF CAREER grant no. ECCS-1749177. J.S. acknowledges support from NSFC (11774035 and 11674032).

Author contributions

L.S. led the optical experiments. C.-Y.W. synthesized the silver plates and fabricated the metasurface. A.K. performed the simulations. J.C., J.S. and A.Z. assisted with experiments. L.S., C.-Y.W., A.K., X.L. and A.A. wrote the manuscript. X.L., A.A., C.-K.S. and S.G. designed and supervised the project. All authors discussed the results and commented on the manuscript at all stages.

Competing interests

The authors declare no competing interests.

Additional information

Supplementary information is available for this paper at https://doi.org/10.1038/s41566-019-0348-z.

Reprints and permissions information is available at www.nature.com/reprints.

Correspondence and requests for materials should be addressed to A.A. or X.L.

Publisher's note: Springer Nature remains neutral with regard to jurisdictional claims in published maps and institutional affiliations.

Methods

Data analysis. To quantify the valley polarization contrast, we used normalized polarization $\rho = \Delta I / \Sigma I$. There are CCD dark counts in the absence of any photoluminescence signal. The contribution of dark counts to the intensity difference $\Delta I = I_+ - I_-$ is naturally removed in the subtraction. However, the dark counts significantly contribute to the sum in the denominator $\Sigma I = I_+ + I_-$. In quoting $\rho = 18\%$, we subtracted the CCD dark counts following the common practice used in other recent studies[11,26]. To avoid dividing by numbers near zero, a small offset of 80 counts was kept in the denominator (Supplementary Section 13).

In the colour maps of valley polarization contrast, the superscript in ρ^* indicates that the CCD dark counts are not removed from the sum intensity. We made this choice to avoid unphysical fluctuations due to dividing by a small number. Therefore, the ρ^* map in Figs. 3 and 4 in the main text only provides a relative value.

Metasurface fabrication. The metasurface was created on top of a single-crystalline silver crystal synthesized in solutions. The single-crystalline silver crystals exhibit low loss because of its atomically smooth surface and absence of grain boundary. The optical properties of these silver plates have been carefully characterized. It has been shown that SPPs can propagate beyond 100 μm on an unstructured silver plate[27].

Optical measurements. Polarization-resolved photoluminescence images were collected using a home-built micro-photoluminescence set-up. A continuous-wave laser at 532 nm was used to excite the monolayer MoS_2. The polarization of the incident light was controlled by a linear polarizer (GTH5M, Thorlabs) combined with a half-waveplate (WPH10M-532, Thorlabs). The incident laser was focused onto the sample by a ×100 objective lens (Mitutoyo Plan Apo) after reflection by a non-polarizing beamsplitter (BS013 Thorlabs). The photoluminescence was collected by the same objective lens, transmitted through the beamsplitter, a quarter-waveplate (05RP32) and a linear polarizer (LPVIS050) and entered the spectrometer equipped with a CCD camera. To obtain a *k*-space image, an additional lens and iris aperture were placed after the objective lens (Supplementary Section 14).

Numerical simulations. Finite-difference time-domain simulations of the silver–MoS_2 structure were conducted using CST Microwave Studio 2017. CST Microwave Studio is a full-wave 3D electromagnetic field solver based on a finite-integral time-domain solution technique. A non-uniform mesh was used to improve the accuracy near the silver slab where the field was large and inhomogeneous. Measured permittivity data for single-crystalline silver were used[44]. The two-dimensional MoS_2 was modelled as a 0.7-nm-thick dielectric layer with experimentally obtained permittivity[45].

Data availability

The data that support the figures in this paper and other findings of this study are available from the corresponding authors upon reasonable request.

References

44. Wu, Y. et al. Intrinsic optical properties and enhanced plasmonic response of epitaxial silver. *Adv. Mater.* **26**, 6106–6110 (2014).
45. Li, Y. et al. Measurement of the optical dielectric function of monolayer transition-metal dichalcogenides: MoS_2, $MoSe_2$, WS_2, and WSe_2. *Phys. Rev. B* **90**, 205422 (2014).